Mechanics of Curved Crease Origami: One-Degree-of-Freedom Mechanisms, Distributed Actuation by Spontaneous Curvature, and Cross-Talk Between Multiple Folds

Antonio DeSimone[1]
The BioRobotics Institute,
Scuola Superiore Sant'Anna,
viale Rinaldo Piaggio 34,
56025 Pontedera, Italy;
MathLab,
SISSA—International School for Advanced
Studies,
via Bonomea 265,
34136 Trieste, Italy
e-mails: a.desimone@santannapisa.it;
desimone@sissa.it

Luciano Teresi
Department of Industrial Engineering,
Università Roma TRE,
00146 Roma, Italy
e-mail: teresi@uniroma3.it

Origami morphing, obtained with patches of piecewise smooth isometries separated by straight fold lines, is an exquisite art that has already received considerable attention in the mathematics and mechanics literature. Curved fold lines, leading to curved creases and curved pleated structures, introduce the additional complexity of mechanical coupling between the folds. This coupling can be exploited to obtain morphing structures with more robust folding pathways. We discuss one-degree-of-freedom mechanisms and folds actuated by spontaneous curvature (as in the case of hygromorphic multilayered composites), comparing the purely geometric approach to two approaches based on the mechanics of active shells and of active three-dimensional solids. Moreover, we discuss the cooperativity of multiple folds and demonstrate the energetic advantage of synchronous folding over sequential folding. [DOI: 10.1115/1.4068453]

Keywords: computational mechanics, elasticity, structures, origami

1 Introduction

Origami morphing, typically obtained with patches of piecewise smooth isometries separated by straight fold lines, is an exquisite art that has already received considerable attention in the mathematics and mechanics literature.

The variant in which the fold lines are not straight is particularly intriguing. Besides the interest acquired in the fields of art, design, manufacturing, and architecture, mastering curved pleated structures require answering a number of fundamental questions. From the point of view of mechanics, the curvature of the fold lines introduces the opportunities and challenges due to the fact that the folds become mechanically coupled. This can be exploited to engineer complex deployable structures whose folding and unfolding can nevertheless be controlled robustly (i.e., in a foolproof fashion) through the actuation of few degrees-of-freedom (DoFs): we discuss here an important example of a 1 DoF mechanism and of its variant obtained by diffuse actuation via spontaneous curvature. In addition, coupling between the folds can be exploited to engineer morphing structures exhibiting multistability and preferred folding

pathways: as an example, we discuss synchronous versus sequential folding for hyper-extensible tubular structures.

The differential geometry of origami obtained by folding along curves, rather than straight lines, has also been investigated by the mathematical community. While the local geometry of folding along a single curve is well understood (see Sec. 2.1), unraveling the global consequences of nontrivial patterns of fold lines (such as, for example, the case of an annulus with multiple concentric circular fold lines, see Ref. [1]) poses challenges that are still unmet. The key problem here is to understand the cross-talk between the various prescribed fold lines. This question of how a curved fold propagates to the next prescribed fold line is very closely related to the one of how distinct neighboring folds interact mechanically, which is the central question motivating our study.

In this article, we focus on the interplay between the geometry and the mechanics of curved folds, and on the issue of cooperative versus antagonistic interactions among multiple folds. Our approach has been inspired by the large existing literature, from which we single out the following contributions [1–10].

2 Two Motivating Examples: Results Using Geometric Models, Active Shells, and Three-Dimensional Active Solids

We set the stage for our discussion of curved crease origami by first considering two key examples. The first is the analysis of a

---

single fold line shaped as a circular arc and actuated by the folding angle in the center, see Sec. 2.1. Here, the results are proof that this is a 1 DoF mechanism and that there is a maximal extent of the fold line before the (local) construction breaks down because of overlapping of the two folds.
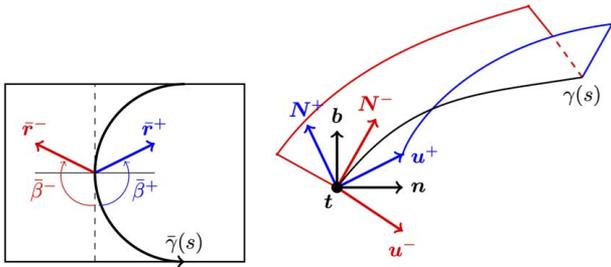
The second motivating example is the analysis of the tapering of two curved pleats separated by a single fold line shaped as a circular arc and actuated by spontaneous (or target) curvature of the pleats, see Sec. 2.2. By "tapering" we mean the increase of the visible curvature of the pleats toward the target value as we move away from the curved crease that joins them. Here, the result is an explanation of the tapered shape predicted by mechanics and observed experimentally in synthetic hygromorphic structures.

The second example, where we consider a mechanism of diffuse actuation throughout the surface of the folding structure should be contrasted against the first one, where actuation is concentrated, through the control of the folding angle at a single point along the fold line.

2.1 Geometric Approach: Actuation by Folding Angle.

In this section, we present the theory for the local geometry of folding along a single curve, and we discuss some of its applications. We start by introducing the notation to describe the geometry of the sheet and the curved fold line, both in the flat state before folding, and in the deformed state reached after the folding has taken place, see Fig. 1, left and right panels, respectively.

We call the *fold line* the planar curve $S \mapsto \bar{\gamma}(S)$, where S is the arc length. We call *ridge* or *crease* its image after deployment by folding, which is a spatial curve $s \mapsto \gamma(s)$, where s is the arc length. Since the deployment map is a (continuous, piecewise) isometry, the map $s = s(S)$ is the identity and s is the arc length on both $\bar{\gamma}$ and γ. The ridge γ separates two regions of a continuous surface with respective normals $\mathbf{N}^+$, $\mathbf{N}^-$, typically shaped as developable strips, which we call *folds* or *pleats*. We denote the Frenet frame along γ with $\{\mathbf{t}, \mathbf{n}, \mathbf{b}\}$ and the Darboux frames with $\{\mathbf{t}, \mathbf{u}^\pm, \mathbf{N}^\pm\}$. Let $\alpha^\pm$ be the angle that brings $\mathbf{n}$ onto $\mathbf{u}^\pm$, see Fig. 2; then we have

$$\mathbf{u}^\pm = \cos\alpha^\pm \mathbf{n} + \sin\alpha^\pm \mathbf{b} \tag{1}$$

The two surfaces joined by the ridge γ may be developable. In this case, we write them as

$$\mathbf{x}(s, v) = \gamma(s) + v\mathbf{r}^\pm(s), \quad v \in [0, \text{ width}^\pm > 0] \tag{2}$$

where the unit vector $\mathbf{r}^+(s)$ (respectively, $\mathbf{r}^-(s)$) gives the direction of the ruling at $\gamma(s)$ on the positive (respectively, negative) side of the surface. Denoting by $\beta^\pm(s)$ the angle that brings $\mathbf{t}(s)$ onto $\mathbf{r}^\pm(s)$, the components of $\mathbf{r}^\pm(s)$ in the Darboux frames $\{\mathbf{t}, \mathbf{u}^\pm, \mathbf{N}^\pm\}$ are $(\cos\beta^\pm, \sin\beta^\pm, 0)$ and hence

$$\mathbf{r}^\pm(s) = \cos\beta^\pm \mathbf{t} + \sin\beta^\pm(\cos\alpha^\pm \mathbf{n} + \sin\alpha^\pm \mathbf{b}) \tag{3}$$

We recall the Frenet formulas for the ridge γ seen as a space curve

$$\frac{d\mathbf{t}}{ds} = \kappa\mathbf{n}, \quad \frac{d\mathbf{n}}{ds} = -\kappa\mathbf{t} + \tau\mathbf{b}, \quad \frac{d\mathbf{b}}{ds} = -\tau\mathbf{n} \tag{4}$$

where κ is the curvature and τ is the torsion, and the Darboux formulas for γ seen as a curve traced on either of the two surfaces with normal $\mathbf{N}^\pm$ (the pleats separated by γ):

$$\frac{d\mathbf{t}}{ds} = \kappa_g^\pm \mathbf{u}^\pm + \kappa_N^\pm \mathbf{N}^\pm, \quad \frac{d\mathbf{u}^\pm}{ds} = -\kappa_g^\pm \mathbf{t} + \tau_r^\pm \mathbf{N}^\pm, \quad \frac{d\mathbf{N}^\pm}{ds} = -\kappa_N^\pm \mathbf{t} - \tau_r^\pm \mathbf{u}^\pm \tag{5}$$

where $\kappa_g^\pm$, $\kappa_N^\pm$, and $\tau_r^\pm$ are geodesic curvature, normal curvature, and relative torsion of γ with respect to the surface with normal $\mathbf{N}^\pm$, see Ref. [11]. For the planar curve $\bar{\gamma}$ (the fold line, namely, the inverse image of the crease γ before folding), formulas (4) and (5) become

$$\frac{d\bar{\mathbf{t}}}{ds} = \bar{\kappa}\bar{\mathbf{u}}, \quad \frac{d\bar{\mathbf{u}}}{ds} = -\bar{\kappa}\bar{\mathbf{t}}, \quad \frac{d\bar{\mathbf{N}}}{ds} = 0 \tag{6}$$
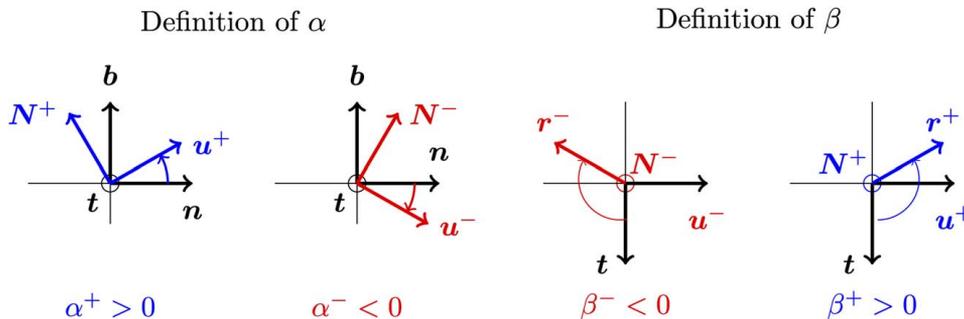
where $\bar{\mathbf{N}}$ is normal to the plane containing the pleats before folding, and $\bar{\mathbf{u}} = \bar{\mathbf{n}}$ is normal to $\bar{\gamma}$.

Folding is realized by a continuous piecewise isometry. This puts stringent constraints on the admissible folded geometries (kinematic compatibility conditions, akin to the Hadamard jump conditions on the gradients of a continuous piecewise affine map). Since isometries preserve distances, angles, and geodesic curvature, we have that

$$\beta^\pm = \bar{\beta}^\pm, \quad \kappa_g^\pm = \bar{\kappa} \tag{7}$$

Then, the continuity of the folding map together with standard results of differential geometry imply

$$\kappa_N^- = \pm\kappa_N^+ \tag{8}$$

Fig. 1 Local geometry of folding along a single curve. Left: flat state before folding, with the 2D fold line $\bar{\gamma}$. Right: deformed state reached after the folding, with the 3D crease γ. Notation and terminology. Frenet frame: t, n, b. Darboux frame: $t, u^\pm, N^\pm$.

Fig. 2 Definition of the angles α and β

and

$$\alpha^- = -\alpha \quad \text{where} \quad \alpha := \alpha^+ \tag{9}$$

so that the dihedral angle of the folded ridge, which we call the *folding angle* θ, is bisected by normal $\mathbf{n}$ and can be written as

$$\theta := \pi - (\alpha^+ - \alpha^-) = \pi - 2\alpha \tag{10}$$

We notice that $\alpha = \pm\pi/2$ corresponds to $\theta = 0, 2\pi$, respectively, and that

$$\kappa = \frac{\bar{\kappa}}{\cos\alpha} \geq \bar{\kappa} \tag{11}$$

Using (9), and since $\tau_r/\kappa_N = \cot\beta$, it follows that (see Refs. [4,11] for details)

$$\cot\beta^\pm = \frac{\tau + (\alpha^\pm)'}{\kappa_g^\pm \tan\alpha^\pm} = \pm\frac{\tau \pm (\alpha)'}{\bar{\kappa}\tan\alpha}$$

and, by adding and subtracting, we deduce that

$$\cot\beta^+ + \cot\beta^- = \frac{2}{\bar{\kappa}}\frac{\alpha'}{\tan\alpha} \tag{12}$$

$$\cot\beta^+ - \cot\beta^- = \frac{2}{\bar{\kappa}}\frac{\tau}{\tan\alpha} \tag{13}$$

Consider now the special case of a piecewise isometry in which the rulings are collinear in the flat state $(\bar{\beta}^+ - \bar{\beta}^- = \pi)$. An example of a physical system realizing this condition is given by foldable containers made of corrugated cardboard, see Fig. 3. Since angles on a surface are preserved by isometries, we also have $\beta^\pm = \bar{\beta}^\pm$ and it follows from (12) and (13) that $\tau = 0$ (hence the folded ridge is always a planar curve!) and

$$\frac{\alpha'}{\tan\alpha} = \frac{\bar{\kappa}}{\tan\beta} = \frac{|\beta'|}{\tan\beta} \tag{14}$$

where $\beta := \bar{\beta}^+$. The ordinary differential equation (ODE) (14) is easily integrated and the profile $\alpha(s)$ is uniquely determined by the initial condition $\alpha(0) = \alpha_0$. This single scalar parameter, which controls the folding angle $\theta = \pi - 2\alpha$ at one point ($s = 0$) of the ridge, uniquely determines the curvature κ of the planar ridge γ via (11) ($\kappa = \bar{\kappa}/\cos\alpha$). The curve γ is then recovered (modulo rigid motions) from the knowledge of κ and $\tau = 0$. The whole pleated structure (one fold) is then reconstructed from (2). In this way, a one-parameter family of curved creases is obtained, parameterized by the angle α_0, which can be continuously unfolded to the flat state (that is, a one-DoF mechanism).

The existence of solutions of ODE (14) in a neighborhood of $s = 0$ guarantees that the sheet can be folded locally along the prescribed fold line $\bar{\gamma}$. The next question is the maximal interval of existence over which this solution can be continued, i.e., the maximal arc length distance s^* over which the sheet can be folded along $\bar{\gamma}$. To explore this question in a concrete example, we consider the special case of a fold line shaped as a circle arc, set $\beta(0) = \beta_0 = \pi/2$ (so that $\beta' < 0$ in a neighborhood of $s = 0$ and the fold line is symmetric with respect to the normal $\bar{\mathbf{n}}(0)$, which leads to a symmetric ridge with respect to the plane generated by $\mathbf{n}(0)$ and $\mathbf{b}(0)$)), and we impose a folding angle $\theta = \pi/2$ at $s = 0$ (hence $\alpha_0 = \pi/4$). By integrating (14) in $(0, s)$, we obtain

$$\sin\alpha(s) = \sin\alpha_0 \frac{1}{\sin\beta(s)} \quad \left(\text{for } \beta_0 = \frac{\pi}{2}\right) \tag{15}$$

where $\beta(s) = \pi/2 - s/R$, and which admits solution with real $\alpha(s)$ for any $\alpha_0 \in (-\pi/2, \pi/2)$ as long as $\sin\beta(s) \geq |\sin\alpha_0|$. At $s = s^\star$ where equality holds, $\alpha(s^\star) = \pm\pi/2$ and the folding angle of the ridge either vanishes or is equal to 2π. We write

$$\alpha(s) = \arcsin\left(\frac{\sin\alpha_0}{\sin\beta(s)}\right), \quad s \in (0, s^\star)$$

and the solution above cannot be continued past $s = s^\star$ without violating noninterpenetration of the two pleats joined by the ridge. For the case $\beta_0 = \pi/2$, this occurs with $\beta(s^\star) = |\alpha_0|$. Figure 4 shows a fold line $\bar{\gamma}$ shaped as a circular sector (arc of a circle) of radius R. If α_0 has to be varied in the interval $(0, \pi/4)$, so that the mechanism at $s = 0$ works as a hinge with folding angle θ closing from π (flat) to $\pi/2$ (in which case the two sides of the ridge are "orthogonal" at $s = 0$), then the maximal length of the fold line is $s^* = R\pi/4$ corresponding to a circular sector with opening angle $\pi/4$ (or $\pi/2$ for its symmetric version).

In practice, the geometric construction described above can be realized in the folding of a sheet if the isometry is rigidly enforced (i.e., if the sheet is unstretchable), and if the direction of the rulings can be prescribed a priori. This second condition can be guaranteed if the bending energy of the sheet is anisotropic so that the sheet is inflexible in one direction (the one of the rulings (3)) and flexible in the perpendicular one with either zero or finite bending modulus $B \geq 0$. This can be obtained, for example, with corrugated cardboard (Fig. 3), with sheets containing embedded stiff and aligned fibers or, to some extent, with sheets made of inflated parallel and unstretchable tubes (see Ref. [5]).

2.2 Mechanical Modeling.

We consider two mechanical models: (1) 2D shell model and (2) 3D solid mechanics. The two models share the same geometric footprint, that is a flat rectangular surface $\mathcal{S} = L \times W$, with the length L and the width W parallel to the X and Y directions, respectively. The 2D region $\mathcal{S}$ is first split into pleats by fold lines (one fold is considered in this section, two and three in the following) and then extruded along the Z direction to a 3D region of thickness H defined by $\mathcal{V} = \mathcal{S} \times (-H/2, +H/2)$. This
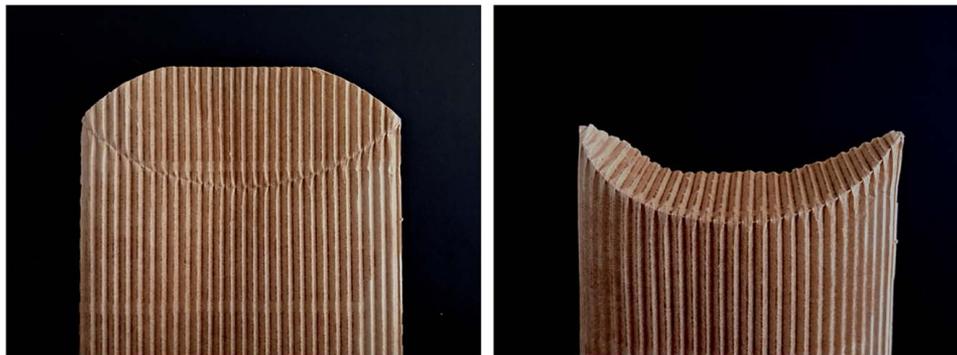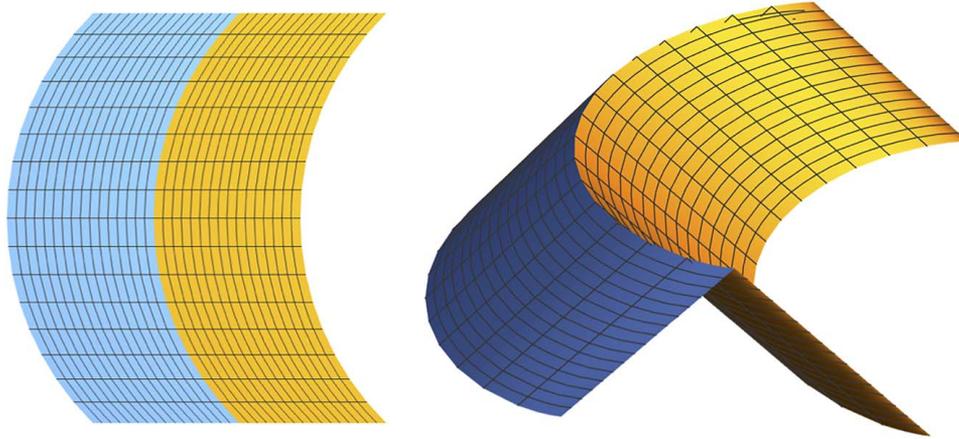

Fig. 3 Example of the circular arc fold line with corrugated cardboard. Flat configuration (left) and curved one (right).

Fig. 4 Example of the circular arc fold line and folded crease obtained with the geometric approach

3D region $\mathcal{V}$ represents the reference configuration of both the 3D solid and the shell-like solid; see Secs. 5.1.1 and 5.1.2 for a brief summary of the theory, and Sec. 5.2 for the details about the geometries.

Mechanical coupling between folds is enforced through kinematic constraints. Adjacent folds are constrained to exhibit identical displacements along the fold line joining them. To enforce this constraint numerically, we observe that each physical fold line is a boundary curve for two adjacent folds, which we conventionally call the left and right folds and fold lines. Denoting the displacements of the left and right folds as $\mathbf{u}_L$ and $\mathbf{u}_R$, respectively, we impose the constraint $\mathbf{u}_R = \mathbf{u}_L$ on the right fold line; reaction forces are then applied to the left fold line to maintain this coupling.

It is worth mentioning that a key characteristic of the constraint is that it solely restricts relative translational motion between the two folds, allowing for independent rotational movement. This is because the shell model's rotational state variables are unconstrained, and controlling linear displacement along a line in the solid model does not restrict relative rotations. Figure 5 shows the case with two folds; on the left, we have the 2D geometry, with fold lines highlighted as thick lines, and on the right the 3D one.

The next two subsections provide detailed insight into the specific problems we addressed to compare the two modeling approaches. To assess the effectiveness of the models, we conducted tests on various geometries featuring two folds and a circular fold line with varying curvature radii, R_o. We always use the same flat region $\mathcal{S} = L \times W$, with $L = 2\,W$, and thickness $H = L/100$, using a different radius of curvature of the circular fold line: $R_o = 0.6\,W, \ldots, 1.1\,W$.

The specific test geometry considered in these subsections allows us to address the origin of the geometric "tapering" predicted by both mechanics models and observed experimentally in synthetic

hygromorphic structures, see Fig. 6. The prescribed (constant) target curvature is achieved at the edges of the rectangular cross section farthest away from the fold line, see right panel of Fig. 6. Moving toward the fold line, the observed curvature decreases to a reduced value, due to the interference of the fold line, which favors different (nonconstant) values of curvature, as shown by the geometric approach in Sec. 2.1. The existence of fold lines that do not interfere with the prescribed target curvature is further investigated in Sec. 3.

2.2.1 Approach by Active Shell Models: Actuation by Target Curvature. We solve the weak equation (31) using as only input the target curvature χ_o; the deformed configurations are obtained by assigning the target curvature χ_o with only one nontrivial component; we have,

$$\chi_o = \begin{bmatrix} 0 & 0 \\ 0 & \chi_{o,yy} \end{bmatrix}; \quad \text{thus,} \quad \chi_e = \begin{bmatrix} \chi_{xx} & \chi_{xy} \\ \chi_{xy} & \chi_{yy} - \chi_{o,yy} \end{bmatrix} \quad (16)$$

The bending term in the shell energy (30) is zero when $\chi_e = 0$, which is when the actual curvature χ_{yy} is equal to the target $\chi_{o,yy}$; in general, this equality cannot be realized, and the minimum of the energy is obtained with all three terms different from zero; in our models, the bending energy is the leading one.

In particular, for each shell, we solve for the configurations $\mathcal{C}_i$ corresponding to a sequence of n pairs $K_i = (\chi_{oi}, -\chi_{oi})$, where χ_{oi} are the target curvatures assigned to the first fold and $-\chi_{oi}$ the ones of the second fold; χ_{oi} ranges in $(0, \chi_m)\,(1/\mathrm{m})$.

2.2.2 Approach by Three-Dimensional Active Elasticity Models: Actuation by Target Metric. We solve the weak equation (21)
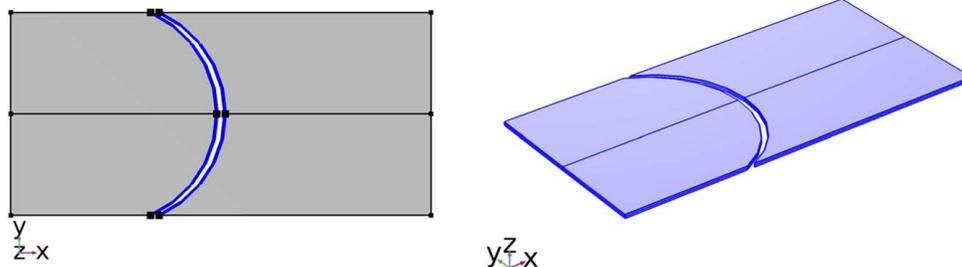
Fig. 5 Geometries with two folds. Left: 2D geometry with two separate folds; the mechanical coupling is obtained by kinematical constraints on the two adjacent fold lines (blue). Right: 3D geometry extruded from the 2D one. The mechanical coupling is obtained by the same kinematical constraints on the fold lines used for the 2D case.
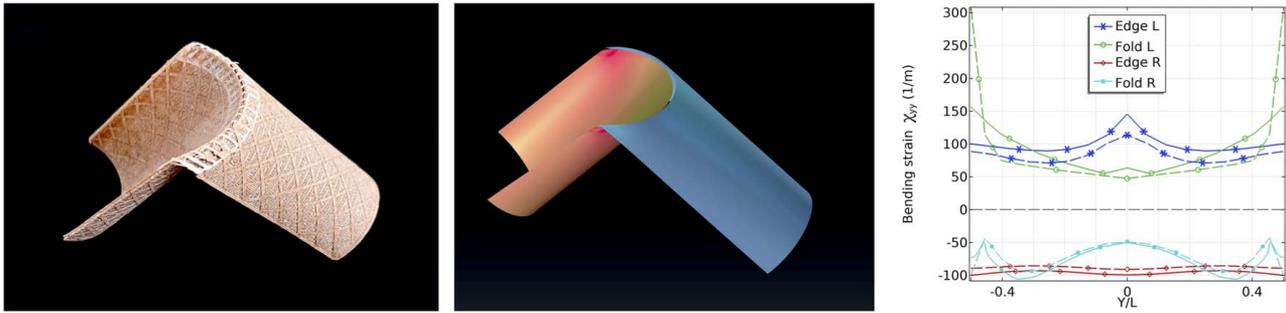
Fig. 6 Left: the hygromorph, courtesy of T. Cheng and Y. Tahouni. Center: result from the shell model; $R_o = 0.6\,W$, $\chi_o = 100\,1/m$. Right: bending strain χ_{yy} versus Y/W along four lines; left (red fold) and right (blue fold) refer to the image at the center. The solid lines correspond to the results obtained from the shell model, whereas the dashed lines correspond to the results from the 3D solid model.
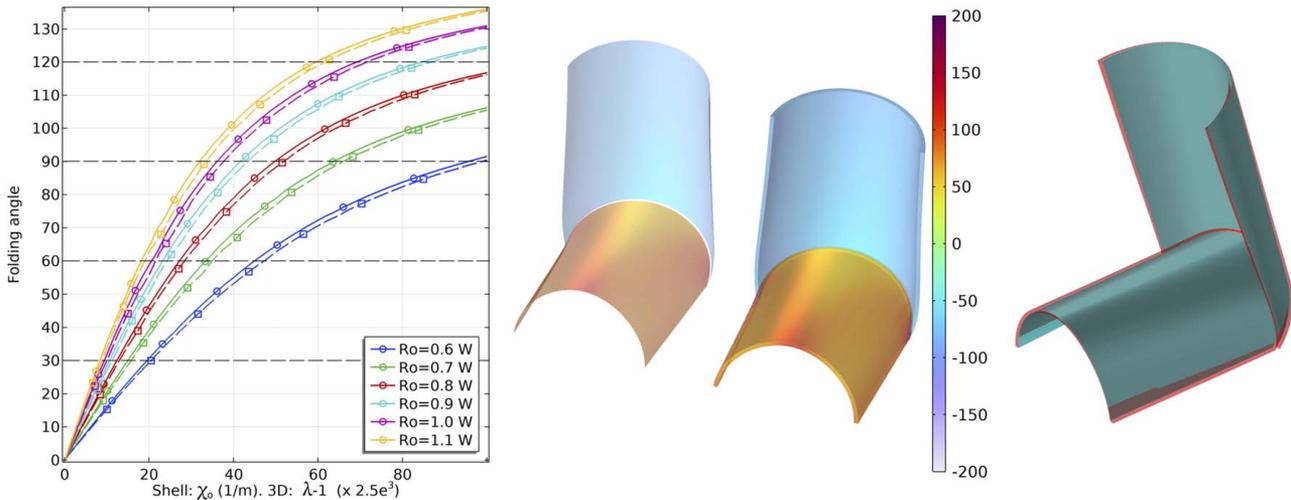
Fig. 7 Comparison of the shell model with the 3D solid model. Left: folding angle θ_{12} versus the target curvature χ_o for the shell model (solid, circle), and versus the target stretch $\lambda_\parallel - 1$ for the 3D model (dashed, square). To align the x-coordinates, we rescale the stretch by $2.5 \times 10^3 (\lambda_\parallel - 1)$. Center: two configurations for $R_o = 0.7\,W$, at $\chi_o = 100\,1/m$ and $\lambda_\parallel - 1 = 0.04$, side by side (left = shell; right = 3D). Right: the previous two configurations superimposed each other.

using as only input a target strain. The deformed configurations are obtained by assigning a target strain $\mathbf{E}_o$ parametrized by the stretch $\lambda_\parallel$, see (19). In particular, each of the two folds is split by a horizontal plane of symmetry in the bottom and top halves; we set $\lambda_\parallel = 1$ in the bottom-left and top-right regions, and we solve for the configurations $\mathcal{C}_i$ corresponding to a sequence of n target stretches $\lambda_i = \lambda_{\parallel i}$, with $\lambda_1 = 1$ and $\lambda_n = \lambda_{max} > 1$; we use a minimal set of kinematical constraints that rule out rigid motions without inducing reactive forces. Figure 7 shows a comparison between the results of the shell model and the 3D model.

3 Role of Geometry of a Single Fold Line: Circular Arcs Versus Trigonometric Functions

Following the modeling approach described in Sec. 2.2.1, we compare the behavior of flat rectangular shells $\mathcal{S} = L \times W$ split into two folds by different fold lines: (1) circular arc and (2) trigonometric function. The geometries are described in Sec. 5.2. The shells are not loaded and have compatible constraints, which means the deformations they exhibit do not generate reaction forces; the only input is the target curvature χ_o, see (16).

For both shells, we solve for the configurations $\mathcal{C}_i$ corresponding to a sequence of n pairs $X_{oi} = (\chi_{oi}, -\chi_{oi})$, where χ_{oi} are the target curvatures assigned to the first fold and $-\chi_{oi}$ the ones of the second fold; χ_{oi} ranges in $(0, \chi_m)\,(1/m)$.

We discuss the results showing: (1) the folding angle $\theta_{12} = 2\,\alpha_{12}$ between the first and the second folds. (2) The actual curvature χ_{yy} of the deformed configuration $\mathcal{C}$ evaluated along the centerline; and (3) the elastic energy density (energy per unit area).

The main result is that for the circular fold line, any value of the target curvature χ_o is incompatible and increases the energy of the shell; see Fig. 8. However, this energy is mostly due to bending (W_b), while the membrane contribution (W_b) is comparatively smaller. As shown in the inset, this is particularly true in the regime of moderate folding angles, the ones smaller than 90 deg where the geometric construction of Sec. 2.1 applies. For completeness, we also show the shear contribution W_s. Conversely, for the trigonometric fold line, there exists a value of the target curvature, and hence of the folding angle, that yields a compatible folding, where also the bending energy vanishes. For this geometry, this special curvature is $\chi_o = 100\,1/m$ and the corresponding folding angle is 110 deg, see Fig. 9. To achieve this folding angle, an energy barrier with significant contributions from both membrane and bending energies needs to be overcome.

We note that using the trigonometric function, it is possible to design a fold line that achieves a compatible configuration at a given value of the target curvature χ_o. In Fig. 10, we show the results corresponding to three different fold lines parametrized by $\vartheta_o = 75\,deg,\ 60\,deg,\ 45\,deg$, at $\chi_o = 100\,1/m$ yields the folding
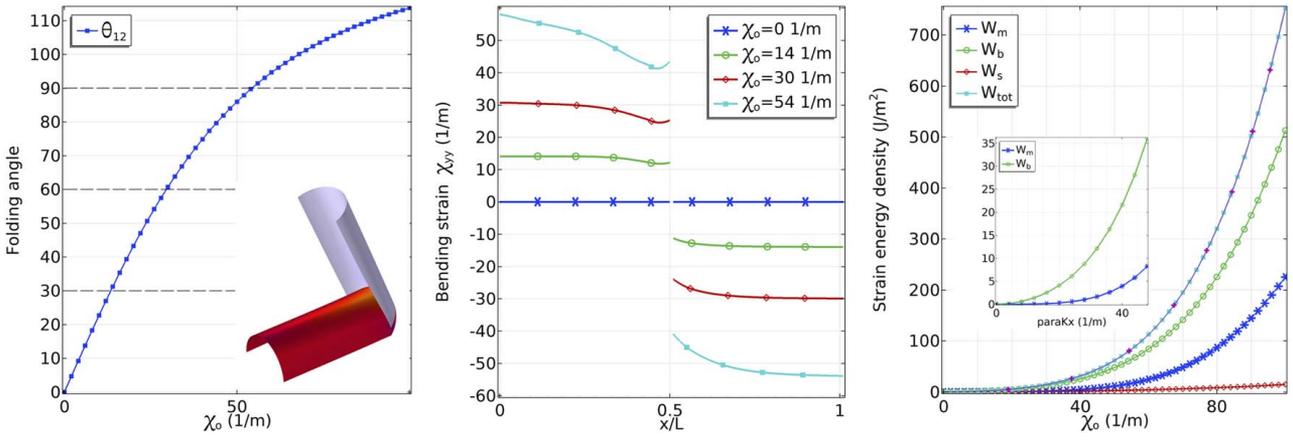
Fig. 8 Result for the circular fold line. Left: folding angle θ_{12} between the two folds; the inset shows the configuration at $\chi_o = 100\,1/m$. Center: current bending strain χ_{yy} versus X/L along the centerline of the shell for three different values of the target curvature χ_o evaluated at the folding angles $\theta_{12} = 30\,deg, 60\,deg, 90\,deg$. It might be noticed that current χ_{yy} differs from the target curvature χ_o as a consequence of the incompatibility of the curvature assigned to the two folds. The difference between χ_{yy} and χ_o increases with the folding angle. Right: elastic energies versus target curvature χ_o; energies increase with χ_o, a consequence of the aforementioned incompatibility of χ_o.
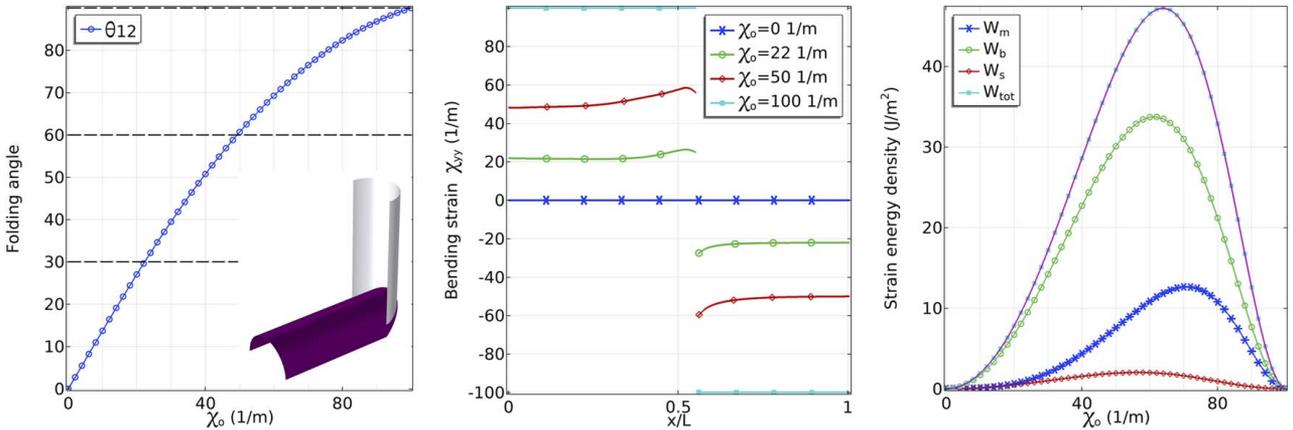
Fig. 9 Result for the trigonometric fold line. Left: folding angle θ_{12} between the two folds; the inset shows the configuration at $\chi_o = 100\,1/m$. Center: current bending strain χ_{yy} versus X/L along the centerline of the shell for three different values of the target curvature χ_o evaluated at the folding angles $\theta_{12} = 30\,deg, 60\,deg, 90\,deg$. It might be noticed that current χ_{yy} differs from the target curvature χ_o as a consequence of the incompatibility of the curvature assigned to the two folds, but contrary to the previous case with circular fold line, at $\theta_{12} = 90\,deg$ we have $\chi_{yy} = \chi_o$, that is $\chi_o = 100\,1/m$ is a compatible target curvature. Right: elastic energies versus target curvature χ_o; it might be noticed that energies are not monotone with χ_o; after increasing, they go back to zero as a consequence of compatibility target curvature $\chi_o = 100\,1/m$.
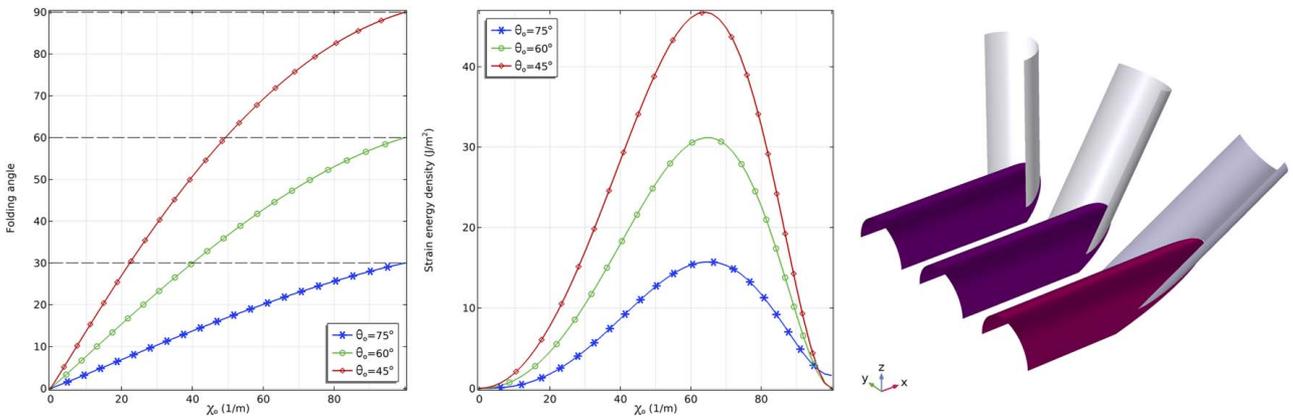
Fig. 10 Result for the trigonometric fold line with three different ϑ_o. Left: folding angle θ_{12} between the two folds; each fold line has been designed to have a compatible configuration at $\chi_o = 100\,1/m$, and with folding angles $\theta_{12} = 30\,deg, 60\,deg, 90\,deg$. Center: elastic energies versus target curvature χ_o; it might be noticed that energies are not monotone with χ_o; after increasing, they go back to zero as a consequence of compatibility target curvature $\chi_o = 100\,1/m$. Right: the three final configurations at $\chi_o = 100\,1/m$.
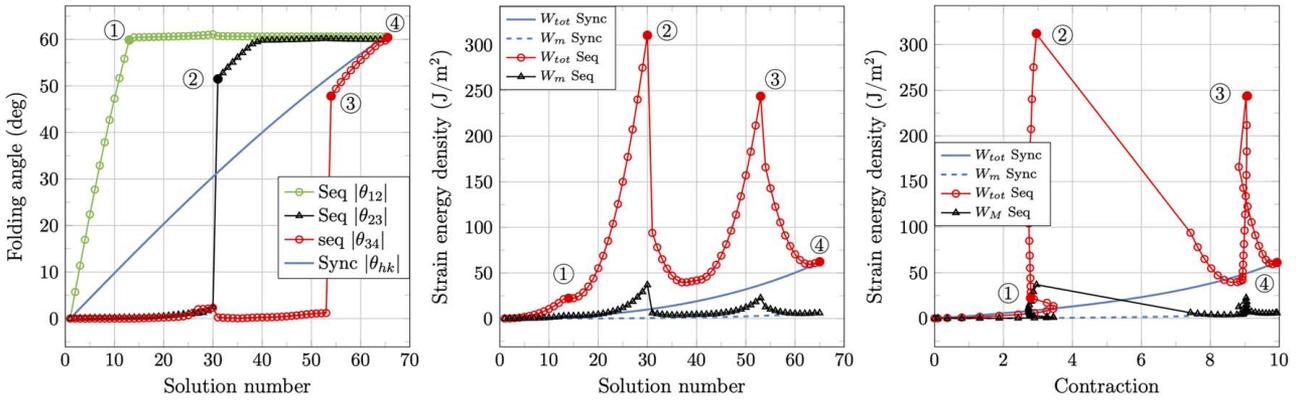
Fig. 11 Comparison of the main results from the synchronous (Sync) and the sequential (Seq) foldings. Left: evolution of the folding angles $|\theta_{hk}|$. Center: evolution of the strain energy density; Seq folding yields nonmonotonic energy, with peaks and valleys, while with Sync folding the energy is a monotonically increasing function. In both cases, membrane energy is much smaller than the total one. Right: strain energy density versus end–end contraction of the shell; it is worth noting the presence of loops where energy increases but contraction decreases. The four numbered points correspond to the configurations in Fig. 12.

angles $\theta_{12} = 30$ deg, 60 deg, 90 deg, respectively. For all three cases, the energy is not monotone with χ_o; after increasing, it goes back to zero as a consequence of the compatibility at $\chi_o = 100\, 1/m$.

4 Interaction Between Folds: Synchronous Versus Sequential Folding in an Array of Four Identical Circular Folds

We consider a flat rectangular shell $\mathcal{S} = L \times W$ split into four folds by three circular fold lines. We look for the configuration associated with the given values of the target curvatures χ_{oj} in each fold $j = 1, \ldots, 4$. In particular, we assign a sequence of n quadruplets

$X_{oi} = (\chi_{01}, \ldots, \chi_{o4})_i$, with $i = 1, \ldots, n$ and χ_{oi} ranging in $(0, \pm \chi_m)$ (1/m), and we solve for the corresponding configuration $\mathcal{C}_i$; we denote with $\theta_{hk} = 2\,\alpha_{hk}$ the folding angle between fold h and k. Two different sequences are used:

- Sync (synchronized): $X_{oi} = (-\chi_{01}, \chi_{01}, -\chi_{01}, \chi_{01})_i$. The alternating sign $\pm$ of the target curvatures in the adjacent folds yields an almost compatible deformation; the change of configuration is smooth and associated with a low increase in elastic energy. The three folding angles exhibit synchronized increases during the process: $|\theta_{12}| = |\theta_{23}| = |\theta_{34}|$.
- Seq (sequential): the whole sequence X_{oi} is split into three subsequences.

$$
\begin{aligned}
X_{oi} &= (-\chi_{01}, \chi_{01}, \chi_{01}, \chi_{01})_i \quad \text{with } \chi_{01} = 0, \ldots, \chi_m, \quad i = 1, \ldots, n_1 \\
X_{oi} &= (-\chi_m, \chi_m, \chi_{03}, -\chi_{03})_i \quad \text{with } \chi_{03} = \chi_m, \ldots, -\chi_m, \quad i = n_1 + 1, \ldots, n_2 \\
X_{oi} &= (-\chi_m, \chi_m, -\chi_m, \chi_{04})_i \quad \text{with } \chi_{04} = -\chi_m, \ldots, \chi_m, \quad i = n_2 + 1, \ldots, n_3
\end{aligned}
\tag{17}
$$

The first sequence changes only the angle θ_{12} between the first fold and the next three. The second one maintains the θ_{12} constant, and only changes θ_{23}; the final sequence maintains both θ_{12} and θ_{23} constant, and changes θ_{34}. The change of configuration might exhibit jumps, and elastic energy is not monotone with the solution number i.

Figure 11 shows a comparison of the main results from the synchronous (Sync) and the sequential (Seq) foldings. Figure 12 contains three panels which compare the main results from the synchronous and the sequential foldings: evolution of the folding angles $|\theta_{hk}|$ (left) and of the strain energy density (center); contraction, which is the distance from the left and the right edge of the shell (right).

5 Interaction Between Folds: Fold Pairs of Circular and Trigonometric Arcs With Different Radii or Heights

Following the modeling approach described in Sec. 2.2.1, we compare the behavior of flat rectangular shells $\mathcal{S} = L \times W$ split into three folds by different pairs of fold lines: (1) two circular arcs, with different curvature radii R_o; (2) two trigonometric function, with different amplitude. The geometries are described in Sec. 5.2. The shells are not loaded and have compatible constraints, that is the deformations they exhibit do not generate reaction forces; the only input is the target curvature χ_o, see (16).

For both shells, we solve for the configurations $\mathcal{C}_i$ corresponding to a sequence of n triplets $X_{oi} = (\chi_{oi}, -\chi_{oi}, \chi_{oi})$, where χ_{oi} are the target curvatures assigned to the first and third folds and $-\chi_{oi}$ the ones of the middle fold; χ_{oi} ranges in $(0, \chi_m)$ (1/m).

We discuss the results showing: (1) the folding angles $\theta_{12} = 2\,\alpha_{12}$ between the first and the second folds, and $\theta_{23} = 2\,\alpha_{23}$ between the second and the third folds, (2) the actual curvature χ_{yy} of the deformed configuration $\mathcal{C}$ evaluated along the centerline, and (3) the elastic energy density (energy per unit area).

The main result is that both geometries exhibit two different folding angles, that is $\theta_{12} \neq \theta_{23}$. Moreover, as already observed, for the circular fold line, any value of the target curvature χ_o is incompatible and increases the energy of the shell; see Fig. 13. Conversely, for the trigonometric fold line, there exists a value of the target curvature that yields a compatible folding: for this geometry, it is $\chi_o = 100\, 1/m$, see Fig. 14.
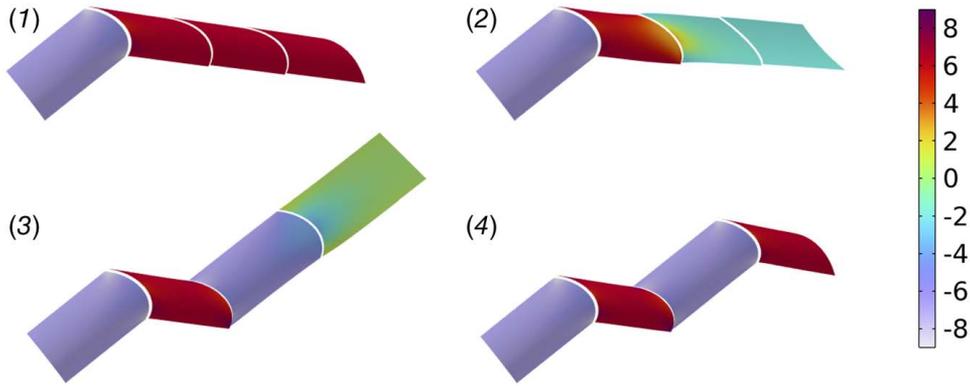
Fig. 12 Four different configurations of the shell made of four folds, undergoing a sequential folding; circular fold lines. Color legend shows the bending strain χ_{yy} in the transversal direction (1/m). The maximum folding angle is 60 deg.
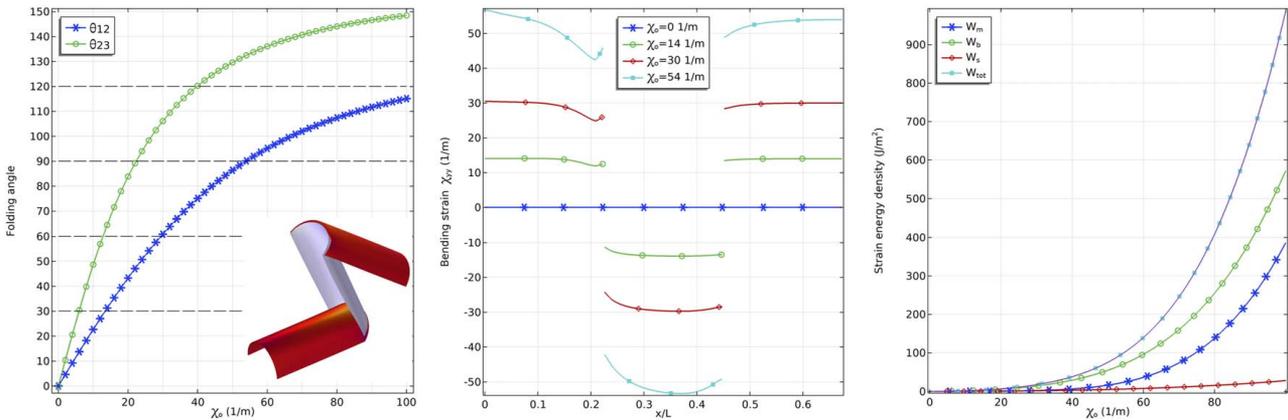

Fig. 13 Result for two different circular fold lines. Left: folding angle θ_{12} and θ_{23} between the two pairs of adjacent folds; we note that for any χ_o there correspond different folding angles. The inset shows the configuration at $\chi_o = 100\,1/m$. Center: current bending strain χ_{yy} versus X/L along the centerline of the shell for three different values of the target curvature χ_o evaluated at the folding angles $\theta_{12} = 30$ deg, 60 deg, 90 deg. It might be noticed that current χ_{yy} differs from the target curvature χ_o as a consequence of the incompatibility of the curvature assigned to the three folds. The difference between χ_{yy} and χ_o increases with the folding angle. Right: elastic energies versus target curvature χ_o; it might be noticed that energies increase with χ_o, a consequence of the aforementioned incompatibility of χ_o.
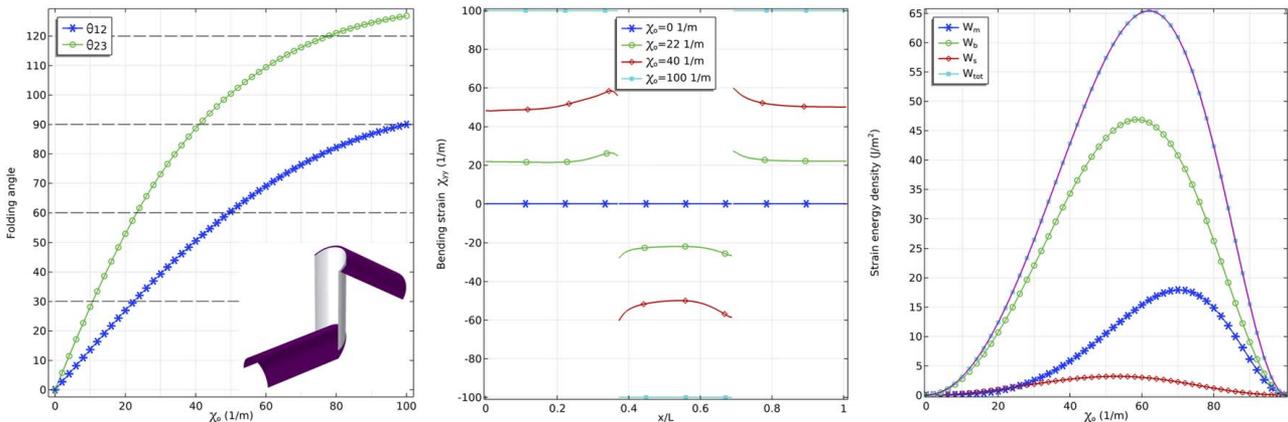

Fig. 14 Result for two different trigonometric fold lines. Left: folding angle θ_{12} and θ_{23} between the two pairs of adjacent folds; we note that for any χ_o there correspond different folding angles. The inset shows the configuration at $\chi_o = 100\,1/m$. Center: current bending strain χ_{yy} versus X/L along the centerline of the shell for three different values of the target curvature χ_o evaluated at the folding angles $\theta_{12} = 30$ deg, 60 deg, 90 deg. The current χ_{yy} differs from the target curvature χ_o as a consequence of the incompatibility of the curvature assigned to the three folds, but contrary to the previous case with circular fold lines, at $\theta_{12} = 90$ deg we have $\chi_{yy} = \chi_o$, that is $\chi_o = 100\,1/m$ is a compatible target curvature for both folds. Right: elastic energies versus target curvature χ_o; the energies are not monotone with χ_o, and after increasing, they go back to zero as a consequence of compatibility at $\chi_o = 100\,1/m$.

5.1 Mechanics Modeling

5.1.1 The Three-Dimensional Model. The reference configuration of the 3D solid is described by $\mathbf{X} = (X, Y, Z)$, where (X, Y, Z) are the material coordinates of $\mathcal{V}$. The current positions $x = (x, y, z)$ of material points X are given by $x = X + \mathbf{u}(X)$, with $\mathbf{u}$ the displacement. The strain $\mathbf{E}$ and stress $\mathbf{S}$ are defined by

$$\mathbf{E} = \frac{1}{2}(\nabla \mathbf{u} + \nabla \mathbf{u}^T + \nabla \mathbf{u}^T \nabla \mathbf{u}), \quad \mathbf{S} = \mathbb{C}\,\mathbf{E}_e, \quad \text{and} \quad \mathbf{E}_e = \mathbf{E} - \mathbf{E}_o \tag{18}$$

where $\mathbb{C}$ is the elastic tensor corresponding to an isotropic material, and $\mathbf{E}_e$ is the elastic strain. The target strain $\mathbf{E}_o$ is defined by

$$\mathbf{E}_o = \lambda_\parallel \, \mathbf{e}_2 \otimes \mathbf{e}_2 + \lambda_\perp (\mathbf{e}_1 \otimes \mathbf{e}_1 + \mathbf{e}_3 \otimes \mathbf{e}_3) \quad \text{with } \lambda_\parallel = 1 + \varepsilon, \quad \lambda_\perp = 1 \tag{19}$$

The target strain $\mathbf{E}_o$ yields a distortion along the Y direction which induces a bending in the plane (Y, Z). The elastic energy Ψ is given by

$$\Psi = \frac{1}{2}\,\mathbb{C}\,\mathbf{E}_e \cdot \mathbf{E}_e \tag{20}$$

Finally, assuming no loads, global energy minimization yields the following weak equation:

$$\int_{\mathcal{V}} \mathbf{S} \cdot \tilde{\mathbf{E}}_e \, dV = 0 \quad \forall \tilde{\mathbf{u}} \tag{21}$$

We solve (21) using as input a sequence of target stretches $\lambda_\parallel = 1, \ldots, \lambda_{\max}$, with a minimal set of kinematical constraints that rule out rigid motions without inducing reactive forces.

5.1.2 The Shell Model. The reference configuration of the shell-like region is given by

$$\mathbb{R}^3 \ni \mathbf{X} = \mathbf{X}(\xi_1, \xi_2, \xi_3) = \mathbf{s}(\xi_1, \xi_2) + \xi_3 \, \mathbf{N}(\xi_1, \xi_2) \tag{22}$$

where $\mathbf{s}: \mathbb{R}^2 \to \mathbb{R}^3$ is the reference shell surface, $\mathbf{N}$ is the shell normal, and ξ_i are the local coordinates on $\mathcal{S}$. The coordinate ξ_3 in the normal direction ranges in $(-H/2, +H/2)$. The state variables of the shell model are the displacement $\mathbf{u}$, yielding the current position of the reference shell surface $\mathcal{S}$, and the vector $\mathbf{a}$ that gives the current normal $\mathbf{n} = \mathbf{N} + \mathbf{a}$. The current configuration of the 3D shell-like region is given by

$$\mathbf{x} = \mathbf{x}(\xi_1, \xi_2, \xi_3) = \mathbf{s}(\xi_1, \xi_2) + \mathbf{u}(\xi_1, \xi_2) + \xi_3 \, \mathbf{n}(\xi_1, \xi_2) \tag{23}$$

Let the indices α and β range in $1, 2$. The in-plane Green-Lagrange strains are measured by

$$\epsilon_{\alpha\beta} = \frac{1}{2}\left(\frac{\partial \mathbf{x}}{\partial \xi_\alpha} \cdot \frac{\partial \mathbf{x}}{\partial \xi_\beta} - \frac{\partial \mathbf{X}}{\partial \xi_\alpha} \cdot \frac{\partial \mathbf{X}}{\partial \xi_\beta}\right)$$
$$= \gamma_{\alpha\beta} + \xi_3 \chi_{\alpha\beta} + O(\xi_3^2) \doteq \gamma_{\alpha\beta} + \xi_3 \chi_{\alpha\beta} \tag{24}$$

The transverse shear is given by

$$\epsilon_{3\alpha} = \epsilon_{\alpha 3} = \frac{1}{2}\left(\frac{\partial \mathbf{x}}{\partial \xi_\alpha} \cdot \mathbf{n} - \frac{\partial \mathbf{X}}{\partial \xi_\alpha} \cdot \mathbf{N}\right) = \zeta_\alpha + O(\xi_3) \doteq \zeta_\alpha \tag{25}$$

Note that the contributions of order $O(\xi_3^2)$ from $\epsilon_{\alpha\beta}$ and order $O(\xi_3)$ from $\epsilon_{3\alpha}$ have been considered negligible, as well as ϵ_{33}. The remaining contributions are called *membrane strain* $\gamma_{\alpha\beta}$, *bending* $\chi_{\alpha\beta}$, and *shear* ζ_α. The membrane stress σ_m, the bending stress σ_b, and the shear stress σ_s are given by

$$\sigma_m = \mathbf{D}\,(\gamma - \gamma_o), \quad \sigma_b = \frac{H}{2}\,\mathbf{D}\,(\chi - \chi_o), \quad \sigma_s = \frac{5}{6}\,2\,G\,(\zeta - \zeta_o) \tag{26}$$

where $\mathbf{D}$ is the 2D plane stress constitutive matrix corresponding to the 3D elastic tensor $\mathbb{C}$, G is the transverse shear moduli, and

γ_o, χ_o, ζ_o are the target or target strains. The current stress σ in the 3D shell-like region is recovered by the formula $\sigma = \sigma_m + z\,\sigma_b$, with z a nondimensional coordinate ranging from -1 (bottom surface) to 1 (top surface). The shell membrane-force $\mathbf{N}_m$, bending moment $\mathbf{M}_b$, and shear force $\mathbf{Q}_s$ are computed from the stresses as follows:

$$\mathbf{N}_m = H\,\sigma_m, \quad \mathbf{M}_b = \frac{H^2}{6}\,\sigma_b, \quad \mathbf{Q}_s = H\,\sigma_s \tag{27}$$

The previous constitutive relations might be rewritten in matrix form as

$$\begin{bmatrix} \mathbf{N}_m \\ \mathbf{M}_b \\ \mathbf{Q}_s \end{bmatrix} = \begin{bmatrix} \mathbf{D}_A & \mathbf{D}_B & 0 \\ \mathbf{D}_B & \mathbf{D}_D & 0 \\ 0 & 0 & \mathbf{D}_{AS} \end{bmatrix} \begin{bmatrix} \gamma_e \\ \chi_e \\ \zeta_e \end{bmatrix} \tag{28}$$

$$\text{with } \gamma_e = \gamma - \gamma_o, \quad \chi_e = \chi - \chi_o, \quad \zeta_e = \zeta - \zeta_o$$

The stiffness matrices in (28) have the following IS units:

$$[\mathbf{D}_A] = \text{N/m}, \quad [\mathbf{D}_B] = \text{N}, \quad [\mathbf{D}_D] = \text{Nm}, \quad [\mathbf{D}_{AS}] = \text{N/m} \tag{29}$$

The elastic energy ψ_{ela} can be represented as the sum of the membrane ψ_m, the bending ψ_b, and the shear energy ψ_s as follows:

$$\begin{aligned} \psi_{ela} &= \psi_m + \psi_b + \psi_s \\ &= 12\,(\mathbf{D}_A\,\gamma_e + \mathbf{D}_B\,\chi_e) \cdot \gamma_e + 12\,(\mathbf{D}_B\,\gamma_e + \mathbf{D}_D\,\chi_e) \cdot \chi_e \\ &\quad + 12\,\mathbf{D}_{AS}\,\zeta_e \cdot \zeta_e \\ &= 12\,\mathbf{N}_m \cdot \gamma_e + 12\,\mathbf{M}_b \cdot \chi_e + 12\,\mathbf{Q}_s \cdot \zeta_e \end{aligned} \tag{30}$$

Finally, assuming no loads, global energy minimization yields the following weak equations:

$$\int_{\mathcal{S}} \left(\mathbf{N}_m \cdot \tilde{\gamma} + \mathbf{M}_b \cdot \tilde{\chi} + \mathbf{Q}_s \cdot \tilde{\zeta}\right) dA = 0 \quad \forall \tilde{\gamma}, \tilde{\chi}, \tilde{\zeta} \tag{31}$$

5.2 Geometries.

We list the shell geometries used to implement and solve our problems. The footprint of each geometry is defined by a rectangle $L \times W$; the shell thickness is $H = L_o/100$. The width W is defined by: $W = \pi \rho_o$ for the circular fold line and $W = 2\,\varphi\,\rho_o$ for the trigonometric fold line. Finally, $\rho_o = 1$, and $h_o = 2\,\rho_o \tan(\vartheta_o)$, $\vartheta_o = 40\,\text{deg}$. The trigonometric fold line is obtained from the oblique section of a right cylinder with a plane (radius ρ_0, angle ϑ_o), by unfolding the cylinder onto a plane, see Fig. 15. For each fold line i, we have: $c_i = $ base point; X_i and Y_i are parametric curves; $s \in (-\varphi, \varphi)$ is the abscissa of the curve.

One Fold: $L = L_o = 2\,W$ or $3\,W$; $R_o = L_o/4$.

- Circular arc; $\varphi = \arcsin(2/3)$.

$$c_1 = (L/4, 0), \quad \begin{cases} X_1 = R_o \, \sin(s + \pi/2) \\ Y_1 = R_o \, \cos(s + \pi/2) \end{cases} \tag{32}$$

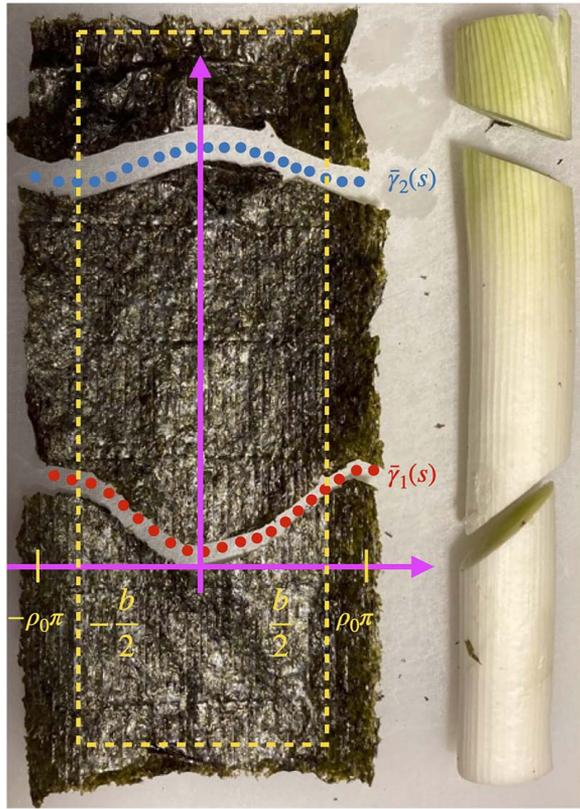- Trigonometric function; $\varphi = \pi/2$.

$$c_1 = (L/2 - h_o/4\,\sin(\varphi), 0),$$
$$\begin{cases} X_1 = h_o/2\,\sin(s + \pi/2) \\ Y_1 = \rho_o\,s \end{cases} \tag{33}$$

Two Folds: $L = 3\,L_o/2$, and $L_o = 3\,W$, $R_o = L_o/4$.

- Circular arc, different folds; $\varphi_1 = \arcsin(2/3)$, $\varphi_2 = \arcsin(1/3)$,

$$c_1 = (L_o/2, 0), \quad \begin{cases} X_1 = R_o \, \sin(s + \pi/2) \\ Y_1 = R_o \, \cos(s + \pi/2) \end{cases}$$
$$c_2 = (L_o, 0), \quad \begin{cases} X_2 = 2\,R_o \, \sin(s + \pi/2) \\ Y_2 = 2\,R_o \, \cos(s + \pi/2) \end{cases} \tag{34}$$

Fig. 15 Illustration of the unfolding of an oblique section of a right cylinder onto a plane, leading to trigonometric fold lines

- Trigonometric function, different folds; $\varphi = \arcsin(2/3)$.

$$c_1 = (L_o/2 - h_o/4 \sin(\phi), 0), \quad \begin{cases} X_1 = h_o/2 \, \sin(s + \pi/2) \\ Y_1 = \rho_o \, s \end{cases}$$

$$c_2 = (L_o - h_o/8 \sin(\phi), 0), \quad \begin{cases} X_2 = h_o/4 \, \sin(s + \pi/2) \\ Y_2 = \rho_o \, s \end{cases}$$

$$\tag{35}$$

Three Folds: $L = 2L_o$, $L_o = 2.82 \, W$, and $W = L_o/2 \sin(\pi/4)$.

- Circular arc, same folds; $\varphi = \pi/4$.

$$c_1 = (L_o/2, 0), \quad c_2 = (L_o, 0), \quad c_2 = (3L_o/2, 0),$$

$$\begin{cases} X_i = L_o/4 \, \sin(s + \pi/2) \\ Y_i = L_o/4 \, \cos(s + \pi/2) \end{cases} \tag{36}$$

Acknowledgment

Conflict of Interest

There are no conflicts of interest.

Data Availability Statement

The datasets generated and supporting the findings of this article are obtainable from the corresponding author upon reasonable request.

References

[1] Alese, L., 2022, "Propagation of Curved Folding: The Folded Annulus With Multiple Creases Exists," Beiträge zur Algebra und Geometrie/Contrib. Algebra Geom., **63**, pp. 19–43.

[2] Demaine, E. D., Demaine, M. L., Huffman, D. A., Koschitz, D., and Tachi, T., "Conic Crease Patterns with Reflecting Rule Lines," 7th International Meeting on Origami in Science, Mathematics and Education (OSME 2018), Oxford, UK, Sept. 5–7.

[3] Feng, F., Dradrach, K., Zmyślony, M., Barnes, M., and Biggins, J. S., 2024, "Geometry, Mechanics and Actuation of Intrinsically Curved Folds," Soft Matter, **20**, pp. 2132–2140.

[4] Fuchs, D., and Tabachnikov, S., 2007, *Mathematical Omnibus: Thirty Lectures on Classic Mathematics*, American Mathematical Society, Providence, RI.

[5] Gao, T., Siéfert, E., DeSimone, A., and Roman, B., 2020, "Shape Programming by Modulating Actuation Over Hierarchical Length Scales," Adv. Mater., **32**, p. 2004515.

[6] Jiang, C., Mundilova, K., Rist, F., Wallner, J., and Pottmann, H., 2019, "Curve-Pleated Structures," ACM Trans. Graph., **38**, pp. 1–13.

[7] Liu, H., and James, R. D., 2024, "Design of Origami Structures With Curved Tiles Between the Creases," J. Mech. Phys. Solids, **185**, p. 105559.

[8] Misseroni, D., Pratapa, P. P., Liu, K., Kresling, B., Chen, Y., Daraio, C., and Paulino, G. H., 2024, "Origami Engineering," Nat. Rev. Methods Primers, **4**, p. 40.

[9] Tachi, T., 2011, "One-dof Rigid Foldable Structures From Space Curves," Proceedings of the IABSE-IASS Symposium, London, UK, Sept. 20–23, pp. 20–23.

[10] Tahouni, Y., Cheng, T., Wood, D., Sachse, R., Thierer, R., Bischoff, M., and Menges, A., 2020, "Self-shaping Curved Folding: A 4d-Printing Method for Fabrication of Self-folding Curved Crease Structures," Proceedings of the 5th Annual ACM Symposium on Computational Fabrication, Virtual, Nov. 5–6, pp. 1–11.

[11] do Carmo, Manfredo P., 1976, *Differential Geometry of Curves and Surfaces*, Prentice-Hall, Englewood Cliffs, NJ.